

Simulation of the influence of energetic atoms on Si homoepitaxial growth

Hartmut Hensel and Herbert M. Urbassek

Fachbereich Physik, Universität Kaiserslautern, Erwin-Schrödinger-Straße, D-67663 Kaiserslautern, Germany

(Received 2 September 1997; revised manuscript received 10 April 1998)

Using a classical molecular-dynamics simulation, we study the homoepitaxial growth on a Si (100) (2×1) surface at 300 K. We compare the structures resulting from the deposition of 2-eV Si atoms, and from a 2% admixture of 30-eV Si atoms. Energetic atom bombardment results in a considerably reduced amorphous layer. This can be shown to be due to the strong bond rearrangement immediately after the energetic atom impact; atom mobility itself is very low. In both simulations, the amorphous layers suffer tensile stress, and an excess of overcoordinated atoms are found. A geometric analysis of the growth of the crystalline phase shows it to be consistent with a well-known structural model of Si recrystallization. [S0163-1829(98)06328-0]

The influence which energetic hyperthermal particles—in the energy range of a few tens of an eV—exert on thin-film growth is of interest for a number of applications such as in growth processes in a plasma environment, or in ion-beam or ion-beam-assisted deposition (IBAD).¹ While it is well known that in growth processes using thermal particles, such as from evaporation sources or in molecular-beam epitaxy (MBE), the resulting structure is mainly influenced by the substrate temperature and the atom arrival rate,² deposition processes using energetic particles offer a higher flexibility in that the energetic particle flux and its energy enter as new parameters. While techniques like IBAD are well established in thin-film growth,¹ the detailed mechanisms by which energetic particles favorably influence epitaxial crystal growth are still under study; this also applies to silicon homoepitaxial growth assisted by energetic particles.³ One of the theoretical means to help in this understanding is an atomistic simulation of the growth processes by means of molecular-dynamics simulation. Its main advantage is that it allows one to trace back all details of the growth process to the interatomic interaction potential. One caveat for the special application of atomistic simulations to growth processes is, however, that the simulated growth occurs on a much faster time scale than in reality, and that in particular all thermal diffusion and relaxation processes occurring in between individual atom arrivals are not represented in the simulation. Nevertheless, it may be hoped that such simulations prove useful in providing insight into microscopic mechanisms of growth processes.^{4–12}

In the present paper, we present computer simulation results on silicon homoepitaxial growth. We use a standard classical molecular-dynamics algorithm, in which Si atoms interact via the Stillinger-Weber potential¹³ with a high-energy modification as provided by Gärtner *et al.*¹⁴ Initially, our crystal consists of eight layers of silicon atoms in diamond structure; we fix the bottom layer and keep the next three layers at a constant temperature of 300 K by a velocity scaling algorithm. Each layer contains 16 atoms under periodic boundary conditions. The crystal is terminated by a (100) (2×1) surface. Two growth scenarios will be considered: (1) At regular intervals of 4 ps, a 2-eV silicon atom drops perpendicularly with random lateral coordinates on the surface. We call this model the MBE scenario in the follow-

ing. (2) We proceed in the same manner as in model (1), but exchange each 48th atom—i.e., that which completes the deposition of the equivalent of 3 ML—by a 30-eV silicon atom. We call this model the IBAD model in the following.

In both scenarios, we deposit the equivalent of 20 ML. Figure 1 displays a cross-sectional view of the resulting Si structures. Evidently, the IBAD scenario leads to an efficient epitaxial crystallization. In fact, we found that on continuing the growth, the thickness of the amorphous layer stays constant at around 5–7 ML, while the remaining material crystallizes epitaxially. The MBE scenario, on the other hand, shows a thick amorphous surface layer; upon continuation of the growth, the amorphous layer grows, and no crystallization takes place. Figure 2 shows the depth-resolved areal density in these structures. In both scenarios, the amorphous phase shows quite large density fluctuations. The amorphous layers contain a considerable fraction (up to 40%) of overcoordinated silicon atoms. They extend throughout the amorphous layer in the MBE scenario, but appear to be more confined to the amorphous-crystalline interface in the IBAD scenario; we also note that the bond-angle distribution in the MBE amorphous phase is slightly broader than in the IBAD amorphous structure. Undercoordinated atoms are mostly confined to the very surface layers, where they by necessity appear; only in the MBE scenario, a few of them (<20%) also appear in deeper layers. We note that the rather high percentage of overcoordinated atoms, which is above that found in relaxed amorphous systems, as well as the considerable density fluctuations are due to the high deposition rate and the corresponding short relaxation times used in our simulation; energetically, however, the amorphous structures produced are quite similar to *a*-Si bulk systems, since their potential energy is around 0.21 eV above that of crystalline silicon, in good agreement with studies of Stillinger-Weber amorphous silicon,¹⁵ which yielded 0.23 eV per atom. Figure 3 displays the stress in the specimens, evaluated according to the recipe of Luedtke and Landman.¹⁶ In both scenarios, the amorphous structure is under considerable tensile stress, which amounts to 10–15 GPa. We presume that this stress is correlated to the large percentage of overcoordinated atoms in our amorphous structure, which is reminiscent of the highly coordinated liquid silicon structure, which also for the Stillinger-Weber potential possesses a higher density than

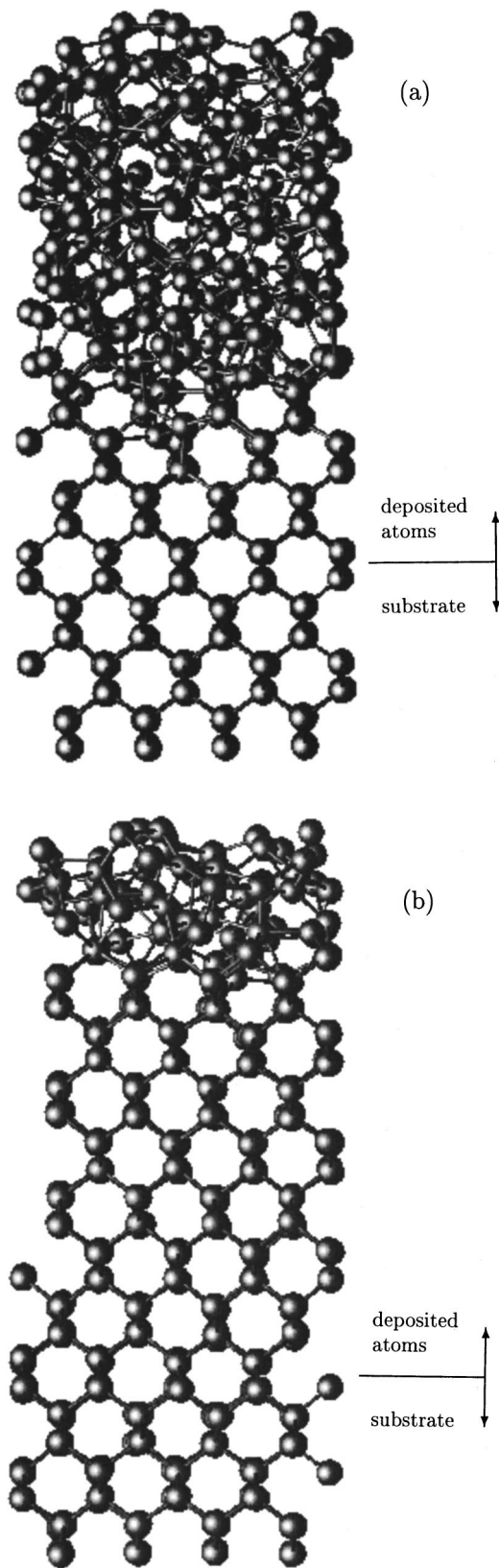


FIG. 1. Cross-sectional view of the deposited film after deposition of an equivalent of 20 ML of Si on a (100) Si substrate. The bottom 7 ML correspond to the original substrate. (a) MBE scenario. (b) IBAD scenario.

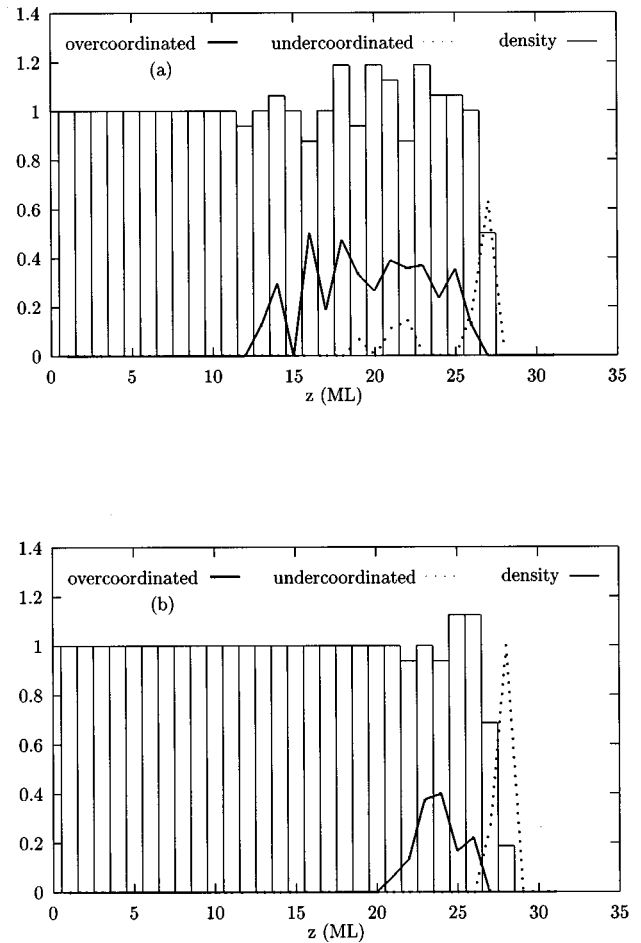


FIG. 2. Areal density (histogram) of the deposited film, relative to the density of *c*-Si, and the fraction of overcoordinated (thick line) and undercoordinated (dashed line) atoms for the MBE scenario (a) and for the IBAD scenario (b).

the crystalline state.¹⁷ This correlation of high coordination with high density may explain the tensile nature of the stress in our overcoordinated amorphous structure with more or less crystalline density.

In order to elucidate how crystallization proceeds, we investigated the bond rearrangements occurring under growth (Fig. 4). To this end we concentrate on the ninth deposited monolayer, which is—even in the MBE growth scenario—the first monolayer that is completely embedded in the amorphous phase. Time $t=0$ starts when the last atom of this monolayer is being deposited. The bonds of ninth-layer atoms are evaluated each time a new monolayer has been deposited. Technically, we assume an atom makes a bond to all surrounding atoms which are closer than the first minimum of the pair correlation function (2.8 Å) in Stillinger-Weber amorphous silicon. It is seen that bond rearrangements in the IBAD scenario are finished when the layer under consideration is buried under six newly deposited layers; this corresponds to the thickness of the amorphous layer, and means that the ninth layer is completely crystallized. In the MBE scenario, on the other hand, bond rearrangements continue; this corresponds to the fact that the ninth layer remains amorphous throughout the simulation. Note also that bond rearrangements are significantly higher in the MBE scenario throughout the deposition process. This suggests that the en-

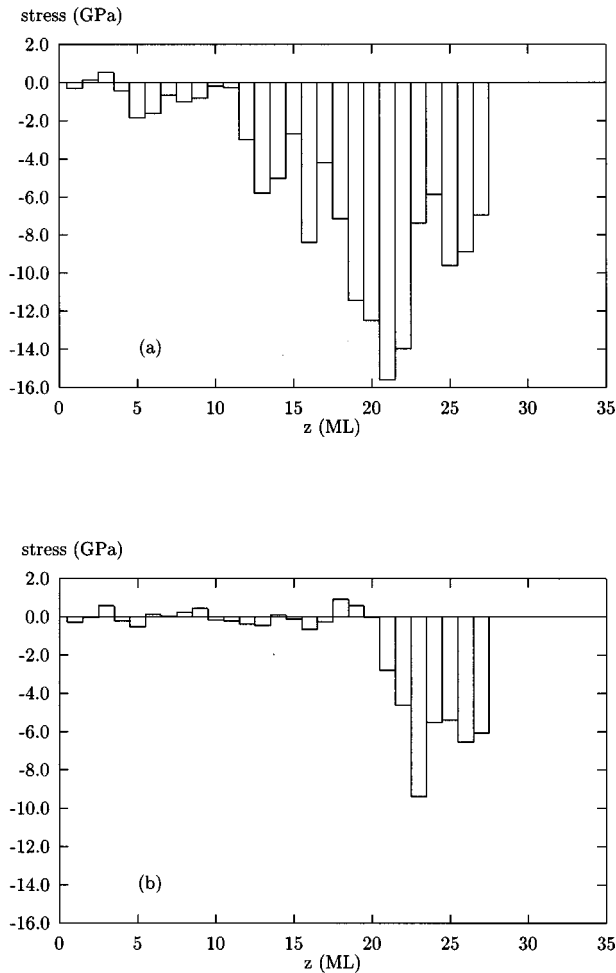


FIG. 3. Stress in the deposited film in the MBE scenario (a) and in the IBAD scenario (b).

energetic particle impinging at time $t=0$ in the IBAD scenario is responsible for most of the structural relaxation (cf. the discussion of Fig. 5 below). Upon close inspection of the data displayed for the IBAD scenario in Fig. 4, a slight enhancement of the bond rearrangement rates at the time when the third layer above the layer under investigation is completed, $t=192$ ps, is seen. If this enhancement can be believed to be statistically significant, it can be nicely correlated with the fact that at this time the next energetic particle has been deposited.

Most interesting is the bond rearrangement rate of layer 9 in the IBAD scenario around the time $t=0$, i.e., when the last particle of this monolayer, which is by definition of our model a 30-eV silicon atom, impinges on the surface. This is shown in Fig. 5, where a tremendous number of bond rearrangements in the freshly deposited surface layer is seen. Such an effect is of course nonexistent in the MBE scenario, and it is responsible for the efficient crystallization in the IBAD scenario, as it evidently leads to a considerable relaxation in the amorphous layer. Note that at time $t=4$ ps, a 2-eV particle is deposited; then no enhancement of bond rearrangements can be observed, in contrast to the 30-eV particle at time $t=0$.

One may wonder whether, besides bond rearrangements, atom mobility plays a role in the amorphous layer and in the crystallization process. To decide this question, we measured

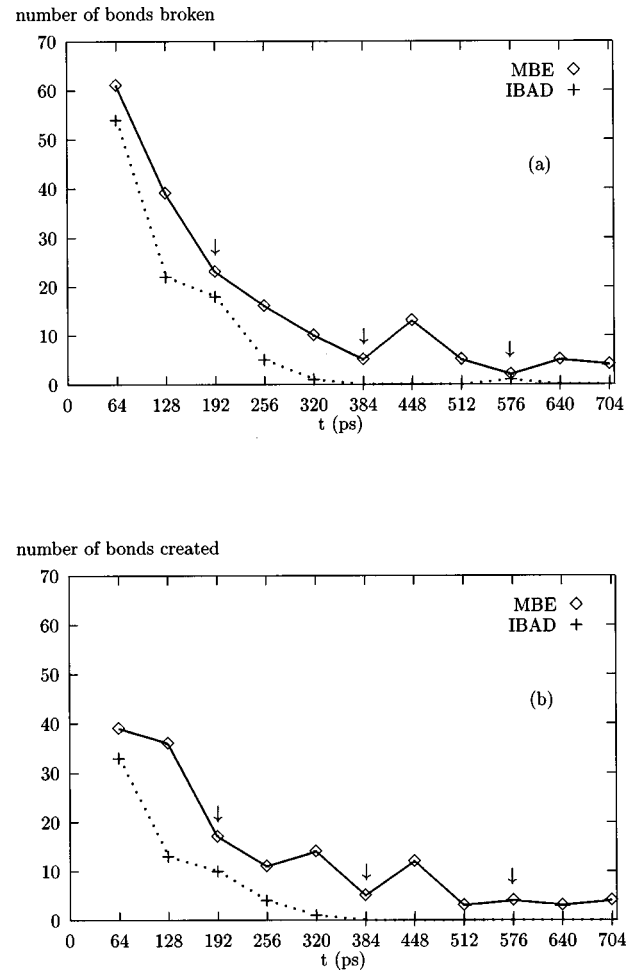


FIG. 4. Number of bonds broken (a) and created (b) during the growth process evaluated for atoms contained in the ninth monolayer of the deposited material. Symbols are given at the times when another full monolayer has been completed; the number of bonds broken, or created, are counted since the completion of the last monolayer. Time is set to $t=0$ when the last atom of monolayer 9 is deposited, which is an energetic atom in the IBAD scenario. An arrow indicates the time when an energetic atom impinges (IBAD scenario).

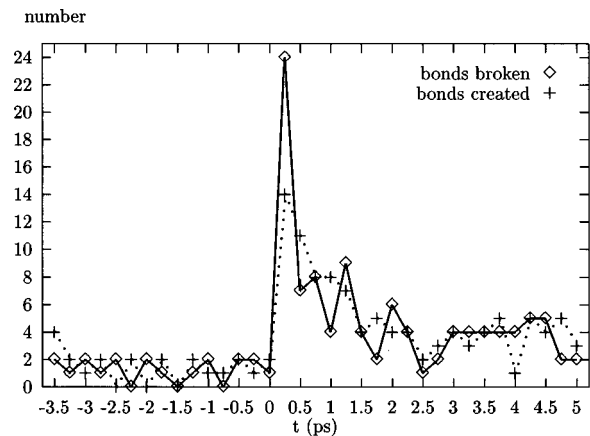


FIG. 5. Number of bonds broken and created in the ninth monolayer in the IBAD scenario around time $t=0$, when an energetic atom impinges. Measurements have been taken every 250 fs; the numbers given denote bonds broken or created since the last measurement.

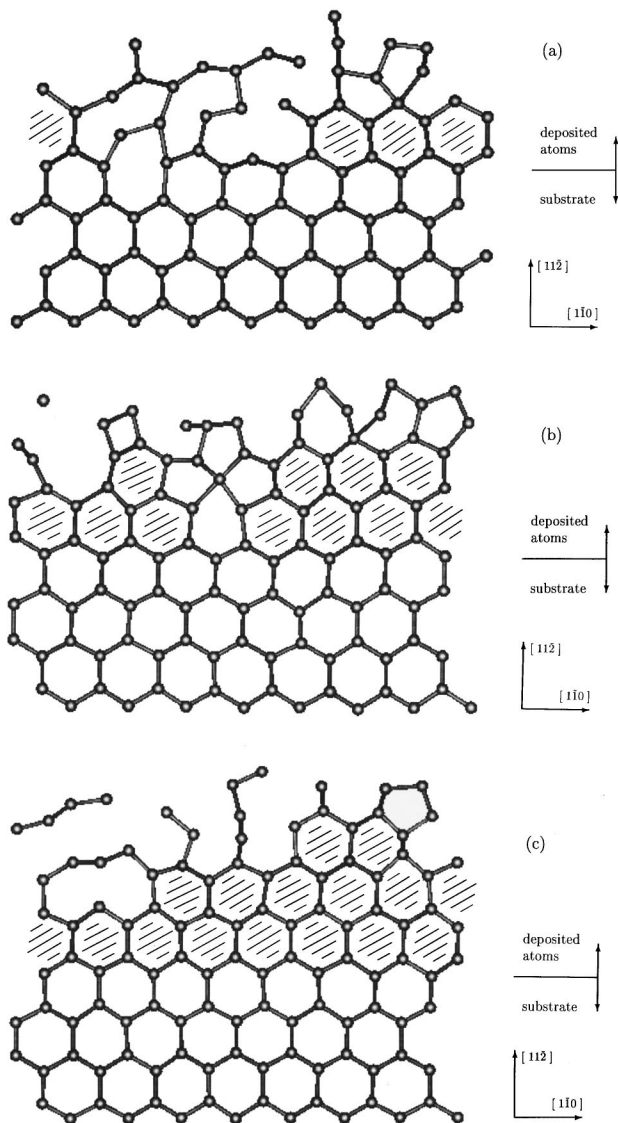


FIG. 6. Growth of the crystalline/amorphous interface into the amorphous phase visualized on a (111) plane; see text. Subfigures (a)–(c) correspond to the deposition of a new monolayer. Hatching shows the crystalline six-atom rings formed.

the mean squared distance covered by ninth-layer atoms, since time $t=0$. The mean squared distance adopted a constant value of around 0.05 \AA^2 (0.07 \AA^2) in the case of MBE (IBAD) growth, on which fluctuations are superimposed. Thus the mean distance which an atom moves is considerably less than the nearest-neighbor distance in silicon, 2.35 \AA . This means that bond rearrangements, which can be performed by minute atom motions, are decisive for crystallization. The difference in atom mobility between the IBAD and MBE scenario is presumably due to the energetic ion impinging at time $t=0$.

Figure 6 gives an atomistic presentation of how the crystalline/amorphous interface proceeds during the deposition. For clarity, this presentation shows a larger crystallite containing 64 atoms per layer; the rate of energetic particles has been increased to $\frac{1}{12}$, since otherwise the amorphous-crystalline interface showed strong deviations from planarity. For this presentation, the crystal is cut along a (111) layer

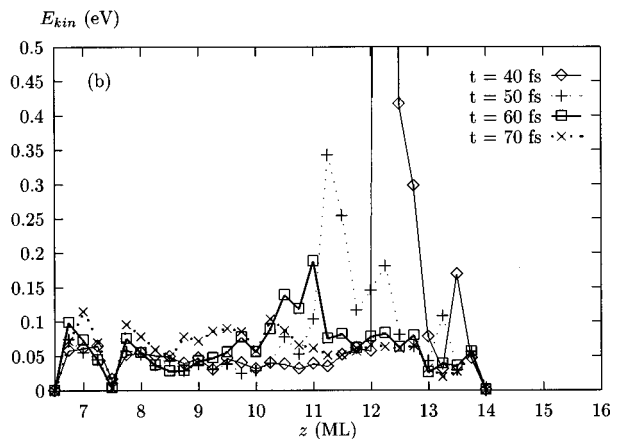
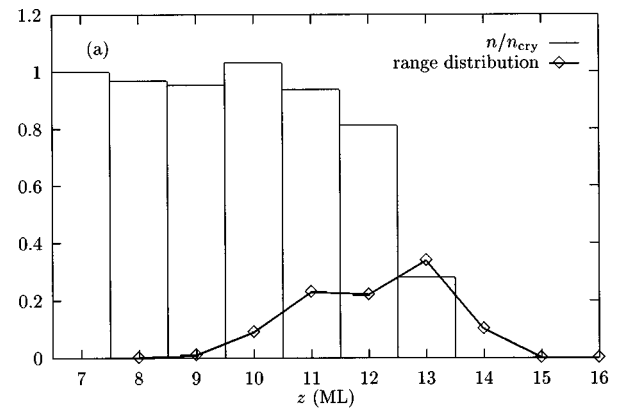


FIG. 7. Range distribution (a) and temporal evolution of kinetic energy per atom (b) of a 30-eV Si ion slowing down in the amorphous top layer of an IBAD-grown Si target. The surface of the original crystalline substrate was at monolayer 7. The density distribution after the deposition of the equivalent of 5 ML is indicated in (a). The material is crystalline below the eighth monolayer.

which leads obliquely from the crystalline to the amorphous phase; all atoms within a slab of thickness 2.4 \AA are shown. This presentation is similar to the one employed by Weber *et al.* in their study of ion-beam-induced crystallization.¹⁸ A series of three stills is shown, which show the same plane after deposition of the fifth, sixth, and seventh monolayers, respectively. The growth of the crystalline phase is here immediately visualized by the completion of the sixfold rings which constitute the building units of the c -Si(111) plane. These figures visualize the so-called structural model proposed by Spaepen¹⁹ and extended by Williams and Elliman,²⁰ who considered kink sites on [110] ledges separating (111) terraces as the sites where crystallization proceeds.^{21,22}

Finally, Fig. 7 demonstrates how the thickness of the amorphous layer in the case of IBAD growth is connected to the properties of the bombarding ion. To this end, we prepare an amorphous film by depositing the equivalent of 5 ML on a crystallite containing 64 atoms per layer. As Fig. 7(a) shows, a 30-eV ion has a rather broad range distribution in the amorphous 5-ML cover layer. This is due to the fact that the surface of the amorphous layer is not atomically flat;

hence ions can be deposited at different depths. Note that the width of the depth distribution coincides rather well with the extent of the amorphous cover layer. No ions penetrate, however, into layers 8 and 9; these present a sort of boundary layer between the amorphous top and the fully crystalline substrate. Figure 7(b) shows us the spatiotemporal evolution of the kinetic-energy profile in the amorphous top layer after deposition of a 30-eV ion. The kinetic energies are averaged over an ensemble of 100 projectiles, and laterally over the cross section of our simulation crystallite. Note that high kinetic energies only occur in the amorphous layer. These two plots demonstrate that the width of the amorphous cover layer is connected to the ion range and its deposited energy.

We finally wish to draw attention to the fact that crystallization depends very sensitively on details of the atomistic interaction potential. In fact, when changing the strength of the three-body interaction potential within the Stillinger-Weber ansatz¹³ (i.e., the parameter λ) by only 5% (i.e., from $\lambda = 21$ to either $\lambda = 20$ or $\lambda = 22$), we observe the amorphous layer formed in an IBAD scenario to have changed from seven layers to either 16 or four layers, respectively. The Stillinger-Weber three-body term determines the energetic costs of deviating from the ideal diamond tetrahedral bond

angles. This sensitive dependence shows how delicately the many-body interaction in silicon, which stabilizes the diamond structure, controls the amorphous phase and also the phase transition between the amorphous and crystalline state.

In summary, we demonstrated by means of a molecular-dynamics simulation the different Si thin-film deposition processes occurring with and without the inclusion of energetic particles among the deposited atoms. Energetic Si atoms lead to an improved epitaxial crystallization of the deposited amorphous layer. Bond rearrangements, rather than atom mobility, were shown to be responsible for the crystallization. An atomistic presentation of the growth process demonstrates it to be in line with a well-known structural model for recrystallization.^{19–22} The amorphous layer formed is overcoordinated and exhibits tensile stress. The number of overcoordinated atoms in the amorphous phase and the magnitude of the stress are reduced by the deposition of energetic atoms.

We acknowledge financial aid from the Deutsche Forschungsgemeinschaft, and discussions with W. Möller, K. Gärtner, and D. Stock.

-
- ¹*Ion Beam Assisted Film Growth*, edited by T. Itoh (Elsevier, Amsterdam, 1989).
- ²J. Y. Tsao, *Materials Fundamentals of Molecular Beam Epitaxy* (Academic, Boston, 1993).
- ³J. W. Rabalais, A. H. Al-Bayati, K. J. Boyd, and D. Marton, *Phys. Rev. B* **53**, 10 781 (1996).
- ⁴M. Schneider, I. K. Schuller, and A. Rahman, *Phys. Rev. B* **36**, 1340 (1987).
- ⁵E. T. Gawlinski and J. D. Gunton, *Phys. Rev. B* **36**, 4774 (1987).
- ⁶R. Biswas, G. S. Grest, and C. M. Soukoulis, *Phys. Rev. B* **38**, 8154 (1988).
- ⁷I. Kwon, R. Biswas, G. S. Grest, and C. M. Soukoulis, *Phys. Rev. B* **41**, 3678 (1990).
- ⁸B. E. Weaire, B. S. Freer, R. L. Headrick, D. J. Eaglesham, G. H. Gilmer, J. Bevk, and L. C. Feldman, *Appl. Phys. Lett.* **59**, 204 (1991).
- ⁹M. V. Ramana Murty and H. A. Atwater, *Phys. Rev. B* **45**, 1507 (1992).
- ¹⁰G. H. Gilmer and C. Roland, *Radiat. Eff. Defects Solids* **130–131**, 321 (1994).
- ¹¹G. H. Gilmer and C. Roland, *Appl. Phys. Lett.* **65**, 824 (1994).
- ¹²B. Strickland and C. Roland, *Phys. Rev. B* **51**, 5061 (1995).
- ¹³F. H. Stillinger and Th. A. Weber, *Phys. Rev. B* **31**, 5262 (1985).
- ¹⁴K. Gärtner, D. Stock, B. Weber, G. Betz, M. Hautala, G. Hobler, M. Hou, S. Sarite, W. Eckstein, J. J. Jimenez-Rodriguez, A. M. C. Perez-Martin, E. P. Andribet, V. Konoplev, A. Gras-Marti, M. Posselt, M. H. Shapiro, T. A. Tombrello, H. M. Urbassek, H. Hensel, Y. Yamamura, and W. Takeuchi, *Nucl. Instrum. Methods Phys. Res. B* **102**, 183 (1995).
- ¹⁵W. D. Luedtke and U. Landman, *Phys. Rev. B* **40**, 1164 (1989).
- ¹⁶U. Landman, W. D. Luedtke, M. W. Ribarsky, R. N. Barnett, and C. L. Cleveland, *Phys. Rev. B* **37**, 4637 (1988).
- ¹⁷M. D. Kluge, J. R. Ray, and A. Rahman, *Phys. Rev. B* **36**, 4234 (1987).
- ¹⁸B. Weber, D. M. Stock, K. Gärtner, and C. Wende, *Radiat. Eff. Defects Solids* **141**, 161 (1997).
- ¹⁹F. Spaepen, *Acta Metall.* **26**, 1167 (1978).
- ²⁰J. S. Williams and R. G. Elliman, *Phys. Rev. Lett.* **51**, 1069 (1983).
- ²¹F. Priolo, C. Spinella, and E. Rimini, *Phys. Rev. B* **41**, 5235 (1990).
- ²²F. Priolo and E. Rimini, *Mater. Sci. Rep.* **5**, 319 (1990).